Nanoscale Advances

ROYAL SOCIETY OF CHEMISTRY

PAPER

View Article Online
View Journal | View Issue

Cite this: *Nanoscale Adv.*, 2022, **4**, 3957

Effect of manganese substitution of ferrite nanoparticles on particle grain structure†

Zichun Yan, [a] Anish Chaluvadi, [ab] Sara FitzGerald, [c] Sarah Spence, [a] Christopher Bleyer,[a] Jiazhou Zhu,‡[b] Thomas M. Crawford,[c] Rachel B. Getman, [b] John Watt, [d] Dale L. Huber [e] and O. Thompson Mefford [*a]

To investigate the influence of manganese substitution on the saturation magnetization of manganese ferrite nanoparticles, samples with various compositions ($Mn_xFe_{3-x}O_4$, x = 0, 0.25, 0.5, 0.75, and 1) were synthesized and characterized. The saturation magnetization of such materials was both calculated using density functional theory and measured *via* vibrating sample magnetometry. A discrepancy was found; the computational data demonstrated a positive correlation between manganese content and saturation magnetization, while the experimental data exhibited an inverse correlation. X-ray diffraction (XRD) and magnetometry results indicated that the crystallite diameter and the magnetic diameter decrease when adding more manganese, which could explain the loss of magnetization of the particles. For 20 nm nanoparticles, with increasing manganese substitution level, the crystallite size decreases from 10.9 nm to 6.3 nm and the magnetic diameter decreases from 15.1 nm to 3.5 nm. Further high resolution transmission electron microscopy (HRTEM) analysis confirmed the manganese substitution induced defects in the crystal lattice, which encourages us to find ways of eliminating crystalline defects to make more reliable ferrite nanoparticles.

Received 31st March 2022
Accepted 29th July 2022

DOI: 10.1039/d2na00200k

rsc.li/nanoscale-advances

Introduction

Metal substituted ferrite nanoparticles ($Me_xFe_{3-x}O_4$, Me = Mn, Co, Ni, and Zn, *etc.*) have been utilized in a variety of biomedical applications, including magnetic hyperthermia,[1,2] drug delivery,[3–6] and magnetic resonance imaging (MRI) contrast agents.[7–10] $Me_xFe_{3-x}O_4$ ferrite has a spinel structure (AB_2O_4) that can be described as a face-centered cubic arrangement of oxygen atoms where substitute metals and iron locate in the tetrahedral (A site) and octahedral (B site) sites. Saturation magnetization is one of the most important characteristic properties of magnetic materials. It represents "how magnetic" the material can be magnetized to become and is directly proportional to the sum of the magnetic moments of the metal cations.[11] As the magnetic moments in A sites and B sites are antiparallel, the total magnetic moment of the ferrite is dependent on the choice of the metal cations and the distribution of cations between A and B sites.[12] Therefore, such a structure offers a great opportunity to tune the saturation magnetization of metal substituted ferrites by changing the composition *via* chemical manipulations.

Among different transition metal ferrites, manganese substituted ferrite nanoparticles have been used for magnetic heating[13–16] and extensively studied as candidates for T_2 MRI contrast agents due to their high saturation magnetizations.[17–23] To investigate the influence of the composition on the properties of manganese substituted ferrite nanoparticles, several variations of the structures have been synthesized and characterized.[24–29] For example, Yang *et al.* reported that the composition of $Mn_{0.43}Fe_{2.57}O_4$ offers the highest saturation magnetization (Ms = 89.5 emu g^{-1}) and optimal T_2 contrast ability of nonstoichiometric manganese ferrite nanoparticles by testing compositions from Mn_0 to $Mn_{1.06}$.[24] Instead of having a maximum saturation magnetization, the study from Li *et al.* showed that for $Mn_xFe_{3-x}O_4$ (x = 0.11, 0.18, 0.29, 0.44, and 0.49), the saturation magnetization minimizes at the composition of x = 0.29 (Ms = 59.3 emu g^{-1}).[29] Another work showed that when increase the manganese content from x = 0.13 to x = 0.36 the saturation magnetization decreased from 81 to 72 emu g^{-1}.[27] Although the manganese ferrite nanoparticles in the three examples mentioned above were synthesized by similar thermal

[a]*Department of Materials Science & Engineering, Clemson University, Clemson, SC 29634, USA. E-mail: mefford@clemson.edu*

[b]*Department of Chemical & Biomolecular Engineering, Clemson University, Clemson, SC 29634, USA*

[c]*Department of Physics and Astronomy, SmartState Center for Experimental Nanoscale Physics, University of South Carolina, Columbia, South Carolina 29208, USA*

[d]*Center for Integrated Nanotechnologies, Los Alamos National Laboratory, Los Alamos, New Mexico, 87545, USA*

[e]*Center for Integrated Nanotechnologies, Sandia National Laboratories, Albuquerque, New Mexico 87185, USA*

† Electronic supplementary information (ESI) available. See https://doi.org/10.1039/d2na00200k

‡ Present address: Suzhou Novartis Technical Development Co., Ltd, Changshu, China.

decomposition methods, there is no consistent relationship between the composition and the saturation magnetization of the manganese ferrite nanoparticles. Therefore, in this study, we wish to better understand how the composition of manganese ferrite influences its saturation magnetization and attempt to explain the discordance with analysis of the nanostructures in the nanoparticles.

Herein, manganese ferrite nanoparticles with precisely controlled size and composition were synthesized *via* thermal decomposition method and magnetic properties were measured afterwards. Density functional theory (DFT) was used to calculate the saturation magnetizations of manganese ferrites with the Mn cations arranged in different interstitial sites within the bulk crystal structure and the results were compared with the experimental results.

Experimental

Materials for particle synthesis

Iron(III) acetylacetonate, manganese(II) acetylacetonate, styrene (≥99%), and divinylbenzene (tech. 80%) were purchased from Sigma Aldrich; oleic acid (90%) was purchased from Fisher Scientific; 1-octadecene (90%), docosane (90%) were purchased from Acros Organics. Ethanol, hexane, acetone, and nitric acid were purchased from BDH. All reagents were used without any further purification.

Synthesis of manganese ferrite nanoparticles using acetylacetonates

The synthetic procedure was adopted from a reported method with adjustment.[30] Briefly, to synthesize manganese ferrite nanoparticles (Acac sample, targeted 10 nm), iron acetylacetonate and manganese acetylacetonate (3 mmol in total) were mixed in 3 mL oleic acid and 5 mL 1-octadecene. The mixture was mechanically stirred and refluxed at 325 °C under constant flow (0.2 L m^{-1}) of nitrogen for 2 hours before cooling down to room temperature. The composition of the nanoparticles was changed by changing the ratio between iron and manganese precursors while keeping the total molarity constant to ensure similar final sizes. The compositions for each batch were aimed at $Mn_xFe_{3-x}O_4$ (x = 0, 0.25, 0.5, 0.75, and 1) and were thus named Mn_x–Acac (x = 0, 0.25, 0.5, 0.75, and 1).

Synthesis of manganese ferrite nanoparticles using oleates

The synthetic method of choice may significantly change the property of the material. It was shown iron oxide nanoparticles can be synthesized with different precursors and the properties of the resulting products can be significantly different.[31] Therefore, in this study, we chose oleate precursors to synthesize 10 nm manganese ferrite nanoparticles besides using acetylacetonate precursors.

The synthetic procedure was adopted from a previous study with changes.[24,32] Briefly, iron(III) oleate (or manganese(II) oleate) were made by reacting 40 mmol ferric chloride (or manganese(II) chloride) salts with 120 mmol sodium oleate (80 mmol for manganese oleate) in a refluxing solvent mixture of hexane (140 mL), ethanol (80 mL), and water (60 mL) for 4 hours. The metal oleates were obtained by evaporating hexane from the upper layer and precipitated by washing with acetone. The final waxy solid was dried in a vacuum oven overnight at room temperature before use. To synthesize 10 nm manganese ferrite nanoparticles, iron(III) oleate and manganese(II) oleate (3 mmol in total) were mixed in 3 mL oleic acid and 15 mL 1-octadecene. The mixture was refluxed and mechanically stirred under nitrogen at 365 °C for 1.5 hours. This series is named Mn_x–oleate-1 (x = 0, 0.25, 0.5, 0.75, and 1).

The size of nanoparticles plays a critical role in affecting the magnetic properties of the ferrite nanoparticles.[33,34] Therefore, larger particles were synthesized with the same oleate precursors. To synthesize 20 nm manganese ferrite particles, 9 mmol metal oleates, 9 mL oleic acid, and 9 mL 1-octadecene were used, and this series is named Mn_x–oleate-2 (x = 0, 0.25, 0.5, 0.75, and 1). After the reaction, the product was washed by mixing the product with 60 mL ethanol and centrifuged at 10 000 rpm for 3 min to precipitate the particles. The washing process was repeated until the supernatant became clear.

Transmission electron microscopy (TEM) analysis

Electron microscopy was conducted at the AMRL EM facility, Clemson University, and the Center for Integrated Nanotechnologies, Sandia National Laboratories. TEM images for size analysis were taken using Hitachi H7830 at 120 kV with 200 mesh carbon-coated copper grids. High-resolution transmission electron microscopy (HRTEM) images were taken on an FEI Titan ETEM 80-300 (FEI, Hillsboro, Oregon) with Image Cs corrector, operating at 300 kV. Energy dispersive X-ray spectroscopy (EDS) mapping was done using Hitachi SU9000 under 60 kV. The images were further analyzed through Image J (NIH, open source). Size distribution was obtained by randomly selecting more than 300 distinct particles from images with a magnification of ×100k.

Vibrating sample magnetometry (VSM)

VSM was done using a physical property measurement system (PPMS, Quantum Design, Inc.) The samples were prepared by fixing the particles in the matrix of poly styrene-divinylbenzene.[35,36] The monomer mixture was cured at 90 °C with azobisisobutyronitrile (AIBN) as initiator and the high temperature and convection will keep the particles evenly distributed. Magnetization curve was measured with a maximum field of 20 000 Oe (1595.4 kA m^{-1}) at 5 K and 300 K, respectively. Inductively coupled plasma optic emission spectroscopy (ICP-OES) was used to determine the mass of metal elements in each sample with sample digestion. The mass of particles was then calculated by assuming the particles have a $Mn_xFe_{3-x}O_4$ structure. The mass of particles was further used for converting measured magnetic moment (emu) to magnetization (emu g^{-1}, A m^2 kg^{-1}). The measured magnetization *versus* field curves were fitted to the Langevin function weighted using a log-normal size suggested by Chantrell *et al.*[37] This method is also described in previous studies.[38–40] In this study, the fitting was done using SPfit, a MATLAB based program that was developed

by GM Saladino.[41,42] The temperature was set to 300 K and the bulk saturation magnetization was set to 446 kA m^{-1}.[43] It should be noted that this model assumes non-interacting particles.

Inductively coupled plasma optic emission spectroscopy (ICP-OES)

Samples were placed into 20 mL scintillation vials and incubated at 500 °C overnight under ambient air. The resulting solids were then dissolved with 70% nitric acid (1 mL) at 100 °C and kept heating until completely dry. Then 10 mL 2% nitric acid was added into each vial and vortexed for 3 min to ensure solvation. The sample solutions were filtered through 0.2 μm syringe filters before measurement. Standard solutions (100 ppm, 50 ppm, 10 ppm, 5 ppm, 1 ppm, and 0.5 ppm) containing iron and manganese were prepared by diluting a standard purchased from VWR. The measurement was conducted with a Thermo Scientific iCAP 7200 ICP-OES in radial mode using the standard instrument operating conditions. Optical emission was monitored at the wavelengths of 259.940 nm (Fe) and 257.610 nm (Mn).

X-ray diffraction (XRD)

Powder X-ray diffraction was performed with a Rigaku Ultima diffractometer. The particles were dispersed in *n*-hexane (approximately 50 mg mL^{-1}) and then dropped on a glass substrate. The particles were then deposited by the evaporation of the solvent. All samples were scanned with 0.5° min^{-1} from 25° to 65° with a copper Kα X-ray ($\lambda = 1.54$ Å). The results were analyzed using PANalytical X'Pert HighScore Plus. The peak broadening caused by the size effect were roughly estimated using Scherrer's equation. More explanation will be found in the results and discussion section.

DFT calculations

Simulated structures were based on the bulk structure of Fe_3O_4 (magnetite). We specifically employed a supercell with an initial stoichiometry of $Fe_{24}O_{32}$. A total of up to eight Mn ions were substituted for Fe in the $Fe_{24}O_{32}$ structure to obtain compositions of $Mn_2Fe_{22}O_{32}$, $Mn_4Fe_{20}O_{32}$, $Mn_6Fe_{18}O_{32}$, $Mn_8Fe_{16}O_{32}$ for both inverse and normal spinel structures (see Fig. S3†). Magnetic moments were calculated with the VASP (Vienna *Ab initio* Simulation Package) software.[44–47] Electron exchange and correlation were treated using the Perdew–Burke–Ernzerhof (PBE)[48] functional with the energies of core electrons being simulated using the projector augmented wave (PAW) pseudopotentials[49,50] to a cut-off energy of 520 eV. All calculations included spin-polarization. The DFT + U formalism[51–54] was utilized to capture the strong coulombic repulsion for 3d electrons on the Mn and Fe atoms and to further prevent the delocalization of electrons in these semiconducting materials. Electronic structures were converged self-consistently until the difference in electronic energies between subsequent steps fell below 10^{-5} eV. Unit cell geometries were converged iteratively until the difference in energy between subsequent steps fell below 10^{-4} eV. Full details about model development, DFT calculations, and conversion of the calculated magnetic moment to saturation magnetization are provided in the ESI.†

Results and discussion

Experimental particle size and composition analysis

To study the influence of manganese content on the magnetic properties of manganese substituted ferrite nanoparticles, we need to have good control of particle size and morphology since these factors also influence the magnetic properties of ferrite nanoparticles. The sizes of the particles were determined by TEM. The results are shown in Table 3 and plotted in Fig. 1 (right). Although the composition of each batch varied, for each series of samples, the particle diameters stayed relatively close to the target. It seems that changing the ratio between the iron precursor and manganese precursor did not play a significant role in changing the overall particle sizes. It is important to exclude the size effect on the magnetic properties to find the relationship between the magnetic properties and the compositions of the particles, thus, the synthetic methods provided good materials for further measurements.

The composition of the nanoparticle samples was measured with EDS and ICP-OES. The two measurements have their own merits. We used EDS mapping to analyze the elemental distribution in the particles, as shown in Fig. 2. Based on the mapping, it appears that both iron and manganese are evenly distributed in all the particles of $Mn_{0.75}$–Acac. ICP-OES measures the overall mass of metal elements in the digested sample, while EDS gives the relative amount of each element at a microscopic level. This means that both ICP-OES and EDS can be used for calculating the composition of the particle samples if we assume a $Mn_xFe_{3-x}O_4$ formula. Taking the Acac series as an example, as shown in Table 1 and Fig. 3, both ICP-OES and EDS data are close to the targeted composition with differences within acceptable error. Therefore, later on, for the two oleate series, we used ICP-OES as a standard method to analyze the composition of each sample, and the results are shown in Table 1. The manganese content in the oleate-1 and oleate-2 series was lower than the targeted level, which was also observed

Table 1 The value of *x* in a $Mn_xFe_{3-x}O_4$ composition calculated from ICP-OES data (EDS data)

	Mn_0	$Mn_{0.25}$	$Mn_{0.5}$	$Mn_{0.75}$	Mn_1
Acac	0.00 (0.00)	0.24 (0.23)	0.42 (0.47)	0.70 (0.68)	1.00 (0.99)
Oleate-1	0.07	0.18	0.32	0.47	0.64
Oleate-2	0.01	0.20	0.35	0.69	0.78

Table 2 Saturation magnetization (VSM) at 300 K of particles of different batches (A m^2 kg^{-1})

	Mn_0	$Mn_{0.25}$	$Mn_{0.5}$	$Mn_{0.75}$	Mn_1
Acac	45.59	42.61	22.67	19.87	12.45
Oleate-1	56.69	56.40	43.34	32.40	23.45
Oleate-2	72.89	62.84	44.99	27.37	25.42

Table 3 Particle diameters measured by TEM in comparison with crystallite diameters and lattice parameters measured by XRD, and magnetic diameters

		TEM mean diameter (nm)	XRD crystallite diameter (nm) (311)	Magnetic diameter (nm)	Lattice parameter (Å) (3 1 1)
Acac	Mn_0	11.0 ± 3.1	3.5	7.3 ± 0.3	8.3
	$Mn_{0.25}$	7.7 ± 2.1	3.9	5.8 ± 0.1	8.4
	$Mn_{0.5}$	7.4 ± 1.5	3.1	4.6 ± 0.2	8.5
	$Mn_{0.75}$	8.3 ± 2.5	3.5	4.2 ± 0.8	8.4
	Mn_1	7.6 ± 2.1	2.7	N/A	8.6
Oleate-1	Mn_0	9.5 ± 0.7	4.9	8.1 ± 0.2	8.3
	$Mn_{0.25}$	10.1 ± 0.7	4.6	7.8 ± 0.3	8.4
	$Mn_{0.5}$	9.4 ± 0.8	3.9	6.4 ± 0.5	8.4
	$Mn_{0.75}$	9.9 ± 0.7	3.7	4.7 ± 0.9	8.5
	Mn_1	9.8 ± 0.8	4.1	N/A	8.4
Oleate-2	Mn_0	20.5 ± 1.3	10.9	15.1 ± 0.6	8.3
	$Mn_{0.25}$	21.0 ± 1.4	9.4	11.0 ± 1.3	8.4
	$Mn_{0.5}$	17.8 ± 1.1	7.6	3.5 ± 0.2	8.4
	$Mn_{0.75}$	23.8 ± 2.8	6.8	N/A	8.5
	Mn_1	20.3 ± 1.6	6.3	N/A	8.5

previously by other authors.[27–29] García-Soriano *et al.* provided a nice comparison to other authors demonstrating this phenomena[28] as well as Lasheras *et al.* using X-ray absorption near edge structure (XANES) to determine the oxidative state of the Mn and Fe ions.[27] The measurement of ICP-OES on the VSM sample is critical to the analysis of the VSM data because the measured magnetic moment is proportional to the total quantity of the magnetic particles in each measured sample. With ICP-OES, the total mass of iron, manganese, and ferrite particles, can be calculated, and the mass of particles was then used to normalize the magnetic moment.

Magnetic measurement

The magnetic moment value measured by VSM is proportional to the total mass of magnetic particles. To know the accurate mass of particles in each sample, the VSM samples are digested and measured by ICP-OES. The magnetization curves are measured with a maximum field of around 1600 kA m^{-1}. An example of the magnetization curves of the 20 nm oleate-2 series is shown in Fig. 4. The magnetization at 5 K is slightly larger than the magnetization at 300 K for each sample. At 300 K, there is no obvious coercivity for the samples measured at 300 K showing a typical superparamagnetic behaviour. As seen in Fig. 4, the saturation magnetization of each sample differed significantly, and the saturation magnetization values at 300 K for all samples are presented in Table 2. To better draw a saturation magnetization–composition relationship, the data are plotted in Fig. 5, along with saturation magnetization values from the DFT calculations (lowest energy structures). It should be noted that the DFT calculations indicate normal spinel structures are lower in energy than inverse spinel at all compositions (see section S4 of the ESI†). In addition, calculations were only made for the extreme cases of purely normal and inverse structures, whereas it is known that Mn substitutions

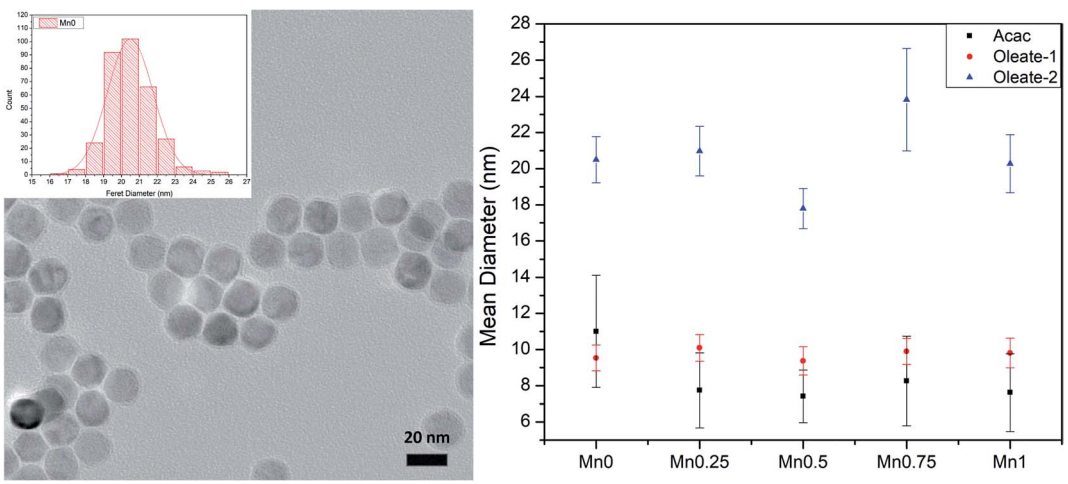

Fig. 1 TEM image and size distribution histogram of Mn_0–oleate-2 (left); the size summary of three series (right). Error bars represent 1 standard deviation from the mean.

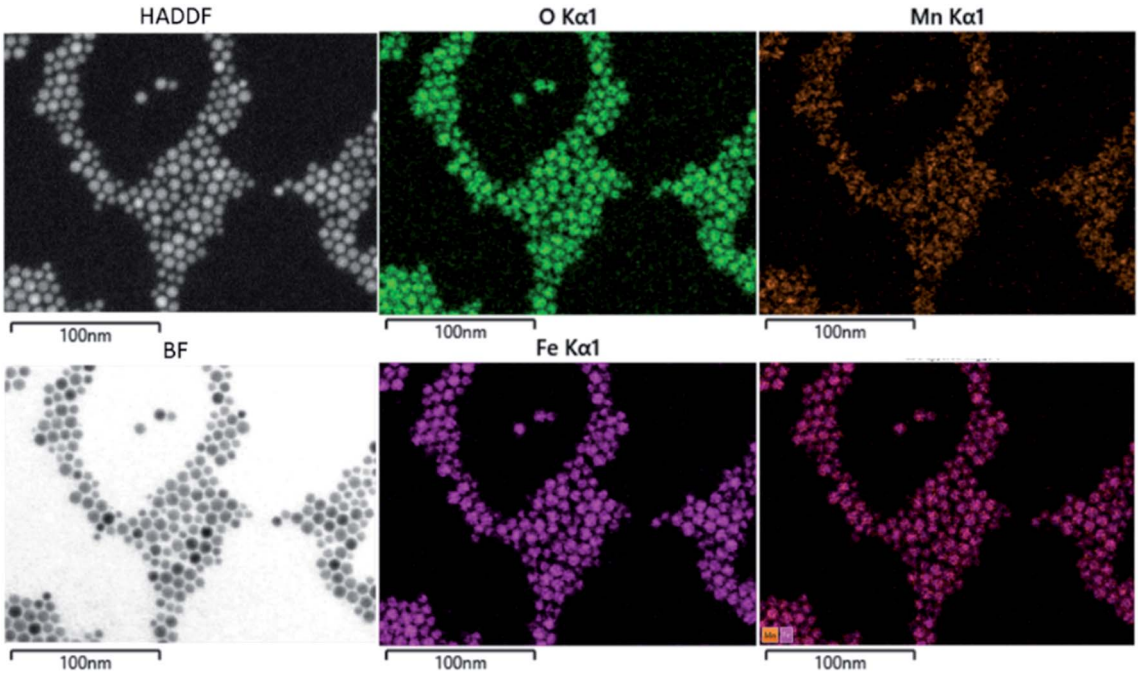

Fig. 2 EDX mapping of $Mn_{0.75}$–Acac sample.

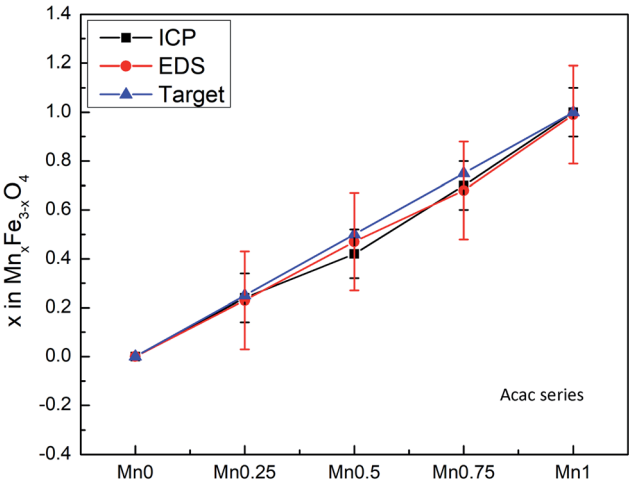

Fig. 3 Comparison between composition measured by ICP-OES and EDS.

typically occur 80% in the A site and 20% in the B site leading to a mix spinel structure.[11] The experimental data showed that for each composition, particles with larger sizes generally had higher saturation magnetizations and for the same size particles the saturation magnetization had a downward trend with the increase of manganese content. The fitted lines are used to show the general trend of the saturation magnetization–composition relationship (does not necessarily mean a linear relationship) for each series of particle samples. In theory, because Mn^{2+} gives the highest magnetic moment among the 3d metals, the incorporation of manganese into the ferrite structure should provide a higher saturation magnetization. However, the experiment produced values were not agreement with the DFT calculations. This finding motivated us to further investigate the influence of composition on saturation magnetization in comparison with the experimental results.

A comparison between computational and experimental (20 nm oleate-2) results is shown in Fig. 5 (right). While the calculated results indicate that the saturation magnetization increases with increasing manganese substitution, consistent with theoretical bulk literature values[11] for manganese ferrites, the opposite relationship is shown for experimental results. As the computational results are based on pristine bulk structures, this led us to investigate the microstructures of the nanoparticles to seek possible explanations for the discrepancy between the computational results and experimental results.

Crystallographic analysis

The origin of the reduction of magnetization of iron oxide was analyzed and reported previously.[31] It seems that the reduction of magnetization is due to the impurities in the crystalline structures of the nanoparticles. To further study the crystal structure of the nanoparticles and explain the discrepancy between the computational and experimental results, the particles were measured by XRD and HRTEM.

The XRD showed that all the samples with different Mn content have a spinel structure (manganese ferrite or magnetite) as shown in Fig. 6. The nano-size of the particles contributes to the peak broadening in the diffractogram significantly, and the crystallite size can be estimated by applying Scherrer's equation: crystallite size $= K\lambda/(\mathrm{FWHM} \times \cos(\theta))$, where K is the shape factor and $K = 0.94$ for this case. FWHM is the full width at the half maximum of the selected peak. λ is the wavelength of

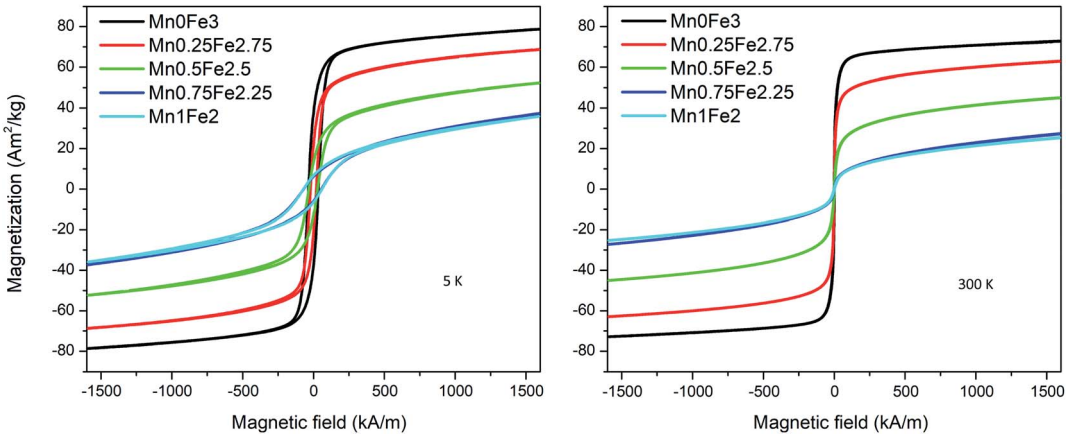

Fig. 4 Magnetization curves of 20 nm oleate-2 samples at 5 K and 300 K.

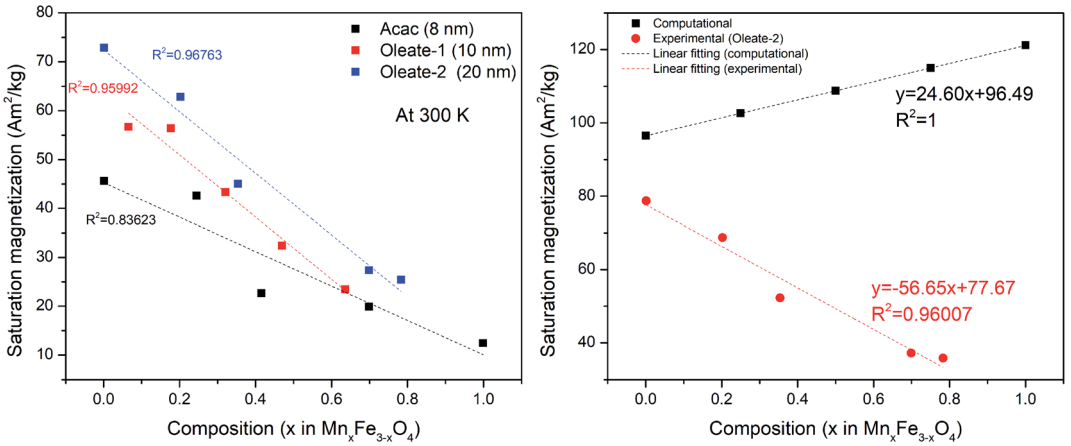

Fig. 5 Saturation magnetization at 300 K of different samples (left). Comparison between computational and experimental (oleate-2, 20 nm) data of different levels of Mn substitution (right).

the X-ray (Cu Kα, 1.54 Å), and θ is the diffraction angle. The lattice parameters can be calculated using Bragg's equation: $d = n\lambda/(2\sin(\theta))$, where d is the interplanar distance and n is the diffraction order. For a face-centered cubic structure, the lattice parameter: $a = \sqrt{(h^2 + k^2 + l^2)/d^2}$, where $(h\ k\ l)$ is the corresponding Miller index of the diffraction plane. The most intense peak at the (311) plane was selected to estimate the crystallite size and lattice parameter, and the results are listed in Table 3. The TEM measured particle sizes, and the fitted magnetic diameters are also shown in Table 3. In general, for each series (Acac, oleate-1, and oleate-2), the crystallite size and the magnetic diameter decrease when the manganese content increases. Some of the samples with high manganese content were unable to properly fit with the program, which is probably due to the extremely small crystallite size and the magnetization curves are too paramagnetic for the program to fit (see ESI† for more information).

The plots in Fig. 7 showed the influence of composition on the crystallite size and the lattice parameter. The fitted lines are only for drawing the general trends and they do not necessarily mean the relationships are linear. Although, there are other factors that may also contribute to the peak broadening, such as microstrain, or instrumental broadening, the broadening caused by crystallite size effect is the most remarkable one and the general trend will be the same if other factors are

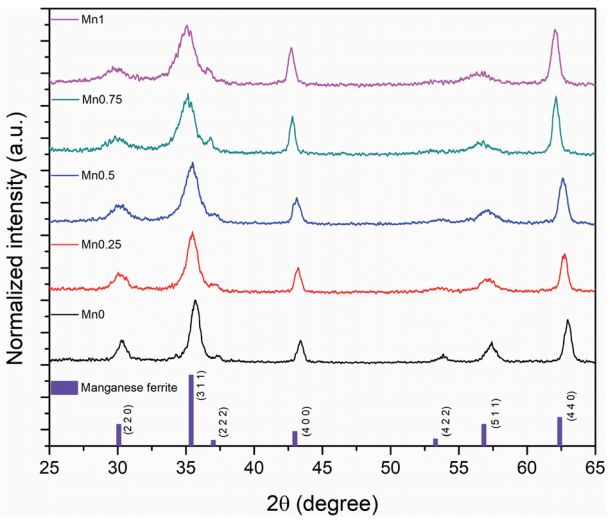

Fig. 6 XRD results of 20 nm oleate-2 samples.

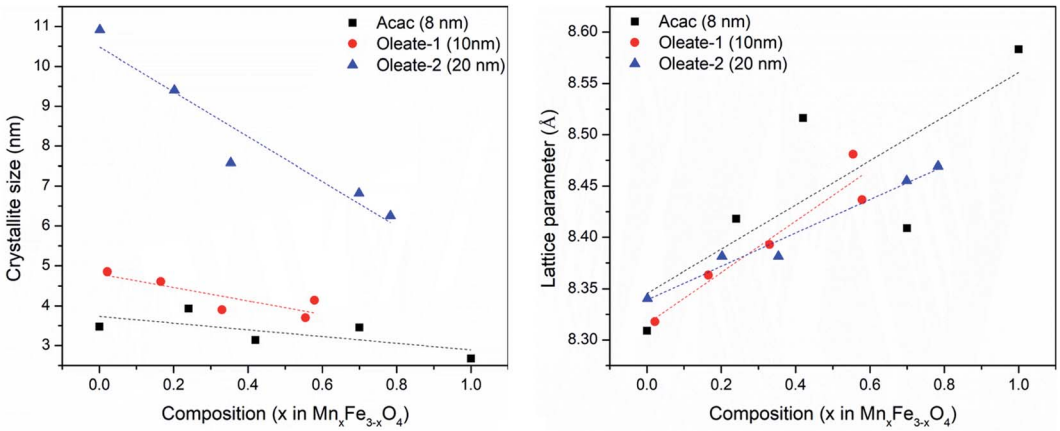

Fig. 7 Crystallite sizes (left) and lattice parameters (right) of different samples calculated from XRD results.

considered. As seen in Fig. 7, regardless of the synthetic method and the size of the particles, for each series, when increasing manganese content, the crystallite size decreased, and the lattice parameters increased. The lattice parameter increase with the metal substitution was previously reported for zinc substitution,[55–57] and for manganese substitution.[29] Comparing to the particle sizes measured by TEM, the crystallite sizes are much smaller. The particles either have very low crystallinity or have polycrystalline structures. Fig. 8 revealed the microstructures inside the 20 nm oleate-2 particles. Fast Fourier Transformation (FFT) of a selected particle showed that the particles are highly crystalline, and the Inverse Fast Fourier Transformation (IFFT) operation on the brightest spot enabled us to see the lattice planes in the particles, as shown in Fig. 8c and f. In the IFFT images, Fig. 8c and f, lattice defects are seen especially for the samples with manganese substitution. It seems that the addition of manganese during the synthesis induced the formation of defects in the crystals and this explains the increase of lattice parameters with manganese substitution. The lattice parameters were calculated from the

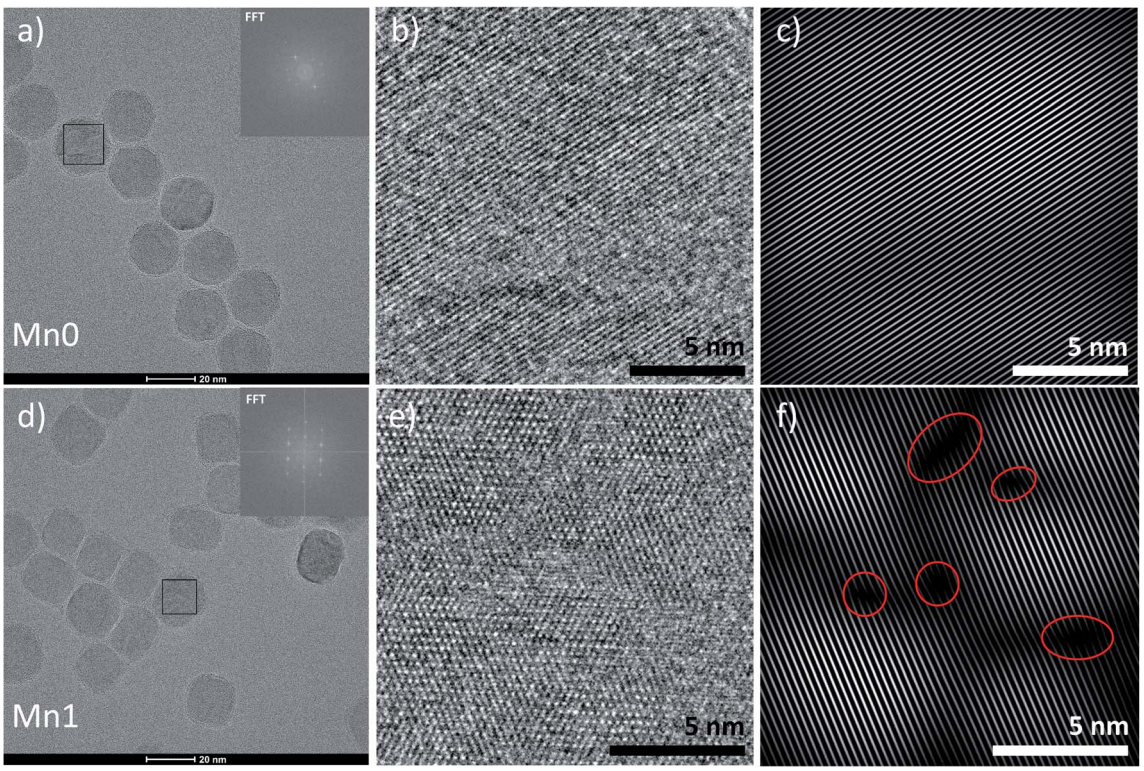

Fig. 8 HRTEM image of 20 nm oleate-2 samples. (a) HRTEM image of Mn_0 oleate-2 and FFT image of the marked area; (b) zoom-in image of the marked area in (a); (c) inverse FFT image of FFT in (b). (d) HRTEM image of Mn_1 oleate-2 and FFT image of the marked area; (e) zoom-in image of the marked area in (d); (f) inverse FFT image of FFT in (e).

peak shift in the XRD diffractograms, which exhibits the overall value of the sum of particles instead of a single particle. Such defects also resulted in smaller crystallite sizes and larger microstrain of the crystals which explains the peak broadening in the XRD results and could also explain the reduction of magnetization of the manganese substituted ferrite particles. Unfortunately, in the previous studies related to substituted ferrite materials, insufficient attention was paid into the control of microstructures of the nanoparticles *via* chemical synthesis, which led to the inconsistency concerning the composition–property relationships as discussed in the introduction. Undoubtedly, more efforts on improving the crystallinity of the synthesized particles are needed to reconcile the experimental results with the computational results. With better control of the crystallinity of the synthesized nanoparticles, more understandings of the structure–property relationship will be explored in the future.

Conclusions

In this study, to study the correlation between the composition of manganese substituted ferrite nanoparticles and their saturation magnetization, nanoparticles were synthesized and characterized with precisely controlled size and compositions. The saturation magnetization was experimentally measured by VSM and calculated with DFT. The computational data suggested that the saturation magnetization increases with increasing the manganese content, while the experimental saturation magnetization becomes lower at higher manganese substitution levels. Further analysis of structure of the nanoparticles indicates that the incorporation of manganese results in the formation of defects in the crystalline structure and the shrinkage of the crystallite size, which lead to the reduction of saturation magnetization of the ferrite particles. This unexpected structure encourages us to put in more efforts to the synthesis of ferrite nanoparticles with minimized crystalline imperfections.

Author contributions

Zichun Yan: project administration, conceptualization, methodology, investigation, data curation, formal analysis, writing – original draft, writing – review & editing. Anish Chaluvadi: conceptualization, methodology, investigation, data curation, writing – original draft, writing – review & editing. Sara Fitz-Gerald: data curation. Sarah Spence: data curation. Christopher Bleyer: data curation, formal analysis. Jiazhou Zhu: conceptualization, methodology. Thomas M. Crawford: supervision, funding acquisition. Rachel B. Getman: supervision, funding acquisition, writing, review, and editing. John Watt: data curation, resources. Dale L. Huber: resources. O. Thompson Mefford: supervision, project administration, funding acquisition, writing – review & editing.

Conflicts of interest

There are no conflicts to declare.

Acknowledgements

This work was performed, in part, at the Center for Integrated Nanotechnologies, an Office of Science User Facility operated for the U.S. Department of Energy (DOE) Office of Science. Los Alamos National Laboratory, an affirmative action equal opportunity employer, is managed by Triad National Security, LLC for the U.S. Department of Energy's NNSA, under contract 89233218CNA000001. Sandia National Laboratories is a multimission laboratory managed and operated by National Technology & Engineering Solutions of Sandia, LLC, a wholly owned subsidiary of Honeywell International, Inc., for the U.S. DOE's National Nuclear Security Administration under contract DE-NA-0003525. The views expressed in the article do not necessarily represent the views of the U.S. DOE or the United States Government. ZY and OTM would like to thank the support by Materials Assembly and Design Excellence in South Carolina (MADE in SC), National Science Foundation award no. OIA-1655740 Grants for Exploratory Academic Research (GEAR). RG and OTM would like to thank the support of National Science Foundation award no. CBET-2146591. The imaging was funded by Clemson Core Incentivized Access (CU-CIA). TMC and SLF acknowledge support from NSF DMR award no. 1808426 and OIA award no. 1655740.

References

1 I. M. Obaidat, B. Issa and Y. Haik, *Nanomaterials*, 2014, **5**, 63–89.
2 C. E. Demirci Dönmez, P. K. Manna, R. Nickel, S. Aktürk and J. Van Lierop, *ACS Appl. Mater. Interfaces*, 2019, **11**, 6858–6866.
3 A. K. Hauser, R. J. Wydra, N. A. Stocke, K. W. Anderson and J. Z. Hilt, *J. Contr. Release*, 2015, **219**, 76–94.
4 E. G. Fuller, H. Sun, R. D. Dhavalikar, M. Unni, G. M. Scheutz, B. S. Sumerlin and C. Rinaldi, *ACS Appl. Polym. Mater.*, 2019, **1**, 211–220.
5 E. Amstad, J. Kohlbrecher, E. Müller, T. Schweizer, M. Textor and E. Reimhult, *Nano Lett.*, 2011, **11**, 1664–1670.
6 M. Pernia Leal, A. Torti, A. Riedinger, R. La Fleur, D. Petti, R. Cingolani, R. Bertacco and T. Pellegrino, *ACS Nano*, 2012, **6**, 10535–10545.
7 I. Fernández-Barahona, M. Muñoz-Hernando, J. Ruiz-Cabello, F. Herranz and J. Pellico, *Inorganics*, 2020, **8**, 1–22.
8 K. R. Hurley, H. L. Ring, M. Etheridge, J. Zhang, Z. Gao, Q. Shao, N. D. Klein, V. M. Szlag, C. Chung, T. M. Reineke, M. Garwood, J. C. Bischof and C. L. Haynes, *Mol. Pharm.*, 2016, **13**, 2172–2183.
9 T. H. Shin, Y. Choi, S. Kim and J. Cheon, *Chem. Soc. Rev.*, 2015, **44**, 4501–4516.
10 H. Bin Na, I. C. Song and T. Hyeon, *Adv. Mater.*, 2009, **21**, 2133–2148.
11 G. C. Cullity BD, B. D. Cullity and C. D. Graham, *Introduction to magnetic materials*, John Wiley & Sons, 2nd edn, 2011.
12 D. S. Mathew and R. S. Juang, *Chem. Eng. J.*, 2007, **129**, 51–65.
13 J. H. Lee, J. T. Jang, J. S. Choi, S. H. Moon, S. H. Noh, J. W. G. Kim, J. W. G. Kim, I. S. Kim, K. I. Park and J. Cheon, *Nat. Nanotechnol.*, 2011, **6**, 418–422.

14 M. Sanna Angotzi, V. Mameli, C. Cara, A. Musinu, C. Sangregorio, D. Niznansky, H. L. Xin, J. Vejpravova and C. Cannas, *Nanoscale Adv.*, 2020, **2**, 3191–3201.
15 Q. Zhang, I. Castellanos-Rubio, R. Munshi, I. Orue, B. Pelaz, K. I. Gries, W. J. Parak, P. Del Pino and A. Pralle, *Chem. Mater.*, 2015, **27**, 7380–7387.
16 L. Del Bianco, F. Spizzo, G. Barucca, M. R. Ruggiero, S. Geninatti Crich, M. Forzan, E. Sieni and P. Sgarbossa, *Nanoscale*, 2019, 10896–10910.
17 S. Xiao, X. Yu, L. Zhang, Y. Zhang, W. Fan, T. Sun, C. Zhou, Y. Liu, Y. Liu, M. Gong and D. Zhang, *Int. J. Nanomed.*, 2019, **14**, 8499–8507.
18 G. Huang, H. Li, J. Chen, Z. Zhao, L. Yang, X. Chi, Z. Chen, X. Wang and J. Gao, *Nanoscale*, 2014, **6**, 10404–10412.
19 J. Lu, S. Ma, J. Sun, C. Xia, C. Liu, Z. Wang, X. Zhao, F. Gao, Q. Gong and B. Song, *Biomaterials*, 2009, **30**, 2919–2928.
20 J. T. Jang, H. Nah, J. H. Lee, S. H. Moon, M. G. Kim and J. Cheon, *Angew. Chem., Int. Ed.*, 2009, **48**, 1234–1238.
21 M. Zhang, Y. Cao, L. Wang, Y. Ma, X. Tu and Z. Zhang, *ACS Appl. Mater. Interfaces*, 2015, **7**, 4650–4658.
22 X. Qian, X. Han, L. Yu, T. Xu and Y. Chen, *Adv. Funct. Mater.*, 2020, **30**(3), 1907066.
23 Y. Fu, X. Li, H. Chen, Z. Wang, W. Yang and H. Zhang, *ACS Appl. Bio Mater.*, 2019, **2**, 3613–3621.
24 L. Yang, L. Ma, J. Xin, A. Li, C. Sun, R. Wei, B. W. Ren, Z. Chen, H. Lin and J. Gao, *Chem. Mater.*, 2017, **29**, 3038–3047.
25 A. Pardo, B. Pelaz, J. Gallo, M. Bañobre-López, W. J. Parak, S. Barbosa, P. Del Pino and P. Taboada, *Chem. Mater.*, 2020, **32**, 2220–2231.
26 J. Amighian, E. Karimzadeh and M. Mozaffari, *J. Magn. Magn. Mater.*, 2013, **332**, 157–162.
27 X. Lasheras, M. Insausti, J. M. De La Fuente, I. Gil De Muro, I. Castellanos-Rubio, L. Marcano, M. L. Fernández-Gubieda, A. Serrano, R. Martín-Rodríguez, E. Garaio, J. A. García and L. Lezama, *Dalton Trans.*, 2019, **48**, 11480–11491.
28 D. García-Soriano, R. Amaro, N. Lafuente-Gómez, P. Milán-Rois, Á. Somoza, C. Navío, F. Herranz, L. Gutiérrez and G. Salas, *J. Colloid Interface Sci.*, 2020, **578**, 510–521.
29 D. Li, H. Yun, B. T. Diroll, V. V. T. Doan-Nguyen, J. M. Kikkawa and C. B. Murray, *Chem. Mater.*, 2016, **28**, 480–489.
30 S. Sun, H. Zeng, D. B. Robinson, S. Raoux, P. M. Rice, S. X. Wang and G. Li, *J. Am. Chem. Soc.*, 2004, **126**, 273–279.
31 Z. Nedelkoski, D. Kepaptsoglou, L. Lari, T. Wen, R. A. Booth, S. D. Oberdick, P. L. Galindo, Q. M. Ramasse, R. F. L. Evans, S. Majetich and V. K. Lazarov, *Sci. Rep.*, 2017, **7**, 1–8.
32 J. Park, K. An, Y. Hwang, J. E. G. Park, H. J. Noh, J. Y. Kim, J. H. Park, N. M. Hwang and T. Hyeon, *Nat. Mater.*, 2004, **3**, 891–895.
33 Q. Song and Z. J. Zhang, *J. Am. Chem. Soc.*, 2004, **126**, 6164–6168.
34 A. G. Kolhatkar, A. C. Jamison, D. Litvinov, R. C. Willson and T. R. Lee, Tuning the magnetic properties of nanoparticles, *Int. J. Mol. Sci.*, 2013, **14**(8), 15977–16009.
35 Z. Yan, S. FitzGerald, T. M. Crawford and O. T. Mefford, *J. Phys.: Mater.*, 2021, **4**, 034013.
36 S. H. Petrosko and E. S. Day, *Biomedical nanotechnology: methods and protocols*, Springer, 2017.
37 R. W. Chantrell, J. Popplewell and S. W. Charles, *IEEE Trans. Magn.*, 1978, **14**, 975–977.
38 O. L. Lanier, O. I. Korotych, A. G. Monsalve, D. Wable, S. Savliwala, N. W. F. Grooms, C. Nacea, O. R. Tuitt and J. Dobson, *Int. J. Hyperther.*, 2019, **36**, 687–701.
39 M. Unni, A. M. Uhl, S. Savliwala, B. H. Savitzky, R. Dhavalikar, N. Garraud, D. P. Arnold, L. F. Kourkoutis, J. S. Andrew and C. Rinaldi, *ACS Nano*, 2017, **11**, 2284–2303.
40 L. Maldonado-Camargo, M. Unni and C. Rinaldi, in *Biomedical Nanotechnology*, Springer, 2017, pp. 47–71.
41 G. M. Saladino, B. Hamawandi, C. Vogt, G. K. Rajarao and M. S. Toprak, *Appl. Nanosci.*, 2020, **10**, 1861–1869.
42 G. M. Saladino, *SPfit – Superparamagnetic Fit (v1.0)*, Zenodo, 2019, DOI: **10.5281/zenodo.3244439r**.
43 R. M. Ferguson, K. R. Minard, A. P. Khandhar and K. M. Krishnan, *Med. Phys.*, 2011, **38**, 1619–1626.
44 G. Kresse and J. Furthmüller, *Phys. Rev. B*, 1996, **54**, 11169.
45 G. Kresse and J. Furthmüller, *Comput. Mater. Sci.*, 1996, **6**, 15–50.
46 G. Kresse and J. Hafner, *Phys. Rev. B*, 1994, **49**, 14251.
47 G. Kresse and J. Hafner, *Phys. Rev. B*, 1993, **47**, 558.
48 J. P. Perdew, K. Burke and M. Ernzerhof, *Phys. Rev. Lett.*, 1996, **77**, 3865.
49 J. J. Mortensen, L. B. Hansen and K. W. Jacobsen, *Phys. Rev. B*, 2005, **71**, 35109.
50 G. Kresse and D. Joubert, *Phys. Rev. B: Condens. Matter Mater. Phys.*, 1999, **59**, 1758.
51 A. Rohrbach, J. Hafner and G. Kresse, *J. Phys.: Condens. Matter*, 2003, **15**, 979.
52 O. Bengone, M. Alouani, P. Blöchl and J. Hugel, *Phys. Rev. B*, 2000, **62**, 16392.
53 A. I. Liechtenstein, V. I. Anisimov and J. Zaanen, *Phys. Rev. B*, 1995, **52**, R5467.
54 S. L. Dudarev, G. A. Botton, S. Y. Savrasov, C. J. Humphreys and A. P. Sutton, *Phys. Rev. B*, 1998, **57**, 1505.
55 V. Mameli, A. Musinu, A. Ardu, G. Ennas, D. Peddis, D. Niznansky, C. Sangregorio, C. Innocenti, N. T. K. Thanh and C. Cannas, *Nanoscale*, 2016, **8**, 10124–10137.
56 D. V. Kurmude, R. S. Barkule, A. V. Raut, D. R. Shengule and K. M. Jadhav, *J. Supercond. Nov. Magnetism*, 2014, **27**, 547–553.
57 A. H. Monfared, A. Zamanian, M. Beygzadeh, I. Sharifi and M. Mozafari, *J. Alloys Compd.*, 2017, **693**, 1090–1095.